Short-term Prediction of the Significant Wave Height and Average Wave Period based on VMD-TCN-LSTM Algorithm

Qiyan Ji[1], Lei Han[1] Lifang Jiang[2], Yuting Zhang[1], Minghong Xie[1] and Yu Liu[1,3]

[1]Marine Science and Technology College, Zhejiang Ocean University, Zhoushan 316022, China
5   [2]South China Sea Forecast and Disaster Reduction Center, Ministry of Natural Resources, Guangzhou 510000, China
[3]Southern Marine Science and Engineering Guangdong Laboratory (Zhuhai), Zhuhai 519000, China

Correspondence to: Lei Han (s20070700026@zjou.edu.cn)

Abstract. The present work proposes a prediction model of significant wave height (SWH) and average wave period (APD)
based on variational mode decomposition (VMD), temporal convolutional networks (TCN), and long short-term memory
10   (LSTM) networks. The wave sequence features were obtained using VMD technology based on the wave data from the
National Data Buoy Center. Then the SWH and APD prediction models were established using TCN, LSTM, and Bayesian
hyperparameter optimization. The VMD-TCN-LSTM model was compared with the VMD-LSTM (without TCN cells) and
LSTM (without VMD and TCN cells) models. The VMD-TCN-LSTM model has significant superiority and shows robustness
and generality in different buoy prediction experiments. In the 3-hour wave forecasts, VMD primarily improved the model
15   performance, while the TCN had less influence. In the 12-, 24-, and 48-hour wave forecasts, both VMD and TCN improved
the model performance. The contribution of the TCN to the improvement of the prediction result determination coefficient
gradually increased as the forecasting length increased. In the 48-hour SWH forecasts, the VMD and TCN improved the
determination coefficient by 132.5 % and 36.8 %, respectively. In the 48-hour APD forecasts, the VMD and TCN improved
the determination coefficient by 119.7 % and 40.9 %, respectively.

20   ## 1 Introduction

Ocean waves are crucial ocean physical parameters, and wave forecasts can significantly improve the safety of marine projects
such as fisheries, power generation, and marine transportation (Jain et al., 2011; Jain and Deo, 2006). The earlier wave
forecasting methods that emerged were semi-analytical and semi-empirical, including the Sverdrup-Munk-Bretscheider
(SMB) (Bretschneider, 1957; Sverdrup and Munk, 1947) and Pierson-Neumann-James (PNJ) methods (Neumann and Pierson,
25   1957). However, empirical methods cannot describe sea surface wave conditions in detail. The most widely used methods for
wave forecasts are those of the third-generation wave models, including WAM (Wamdi, 1988), SWAN (Booij et al., 1999;
Rogers et al., 2003), and WAVEWATCH III (Tolman, 2009). Nevertheless, numerical modelling methods must consume
much computational resources and time (Wang et al., 2018).

Neural network methods achieve higher-quality forecasting results that are less time and computationally cost-consuming.
30   Several neural network methods have been widely used for wave forecasts, e.g., artificial neural networks (ANN) (Deo and

Naidu, 1998; Mafi and Amirinia, 2017; Kamranzad et al., 2011; Malekmohamadi et al., 2008; Makarynskyy, 2004), recurrent neural networks (RNN) (Pushpam P. and Enigo V.S., 2020), and long short-term memory (LSTM) networks (Gao et al., 2021; Ni and Ma, 2020; Fan et al., 2020). The prediction model designed using neural network algorithms individually has poor generalization ability due to the strong non-stationarity and non-linear physical relationship of waves.

35   Signal decomposition methods are effective in extracting original data features. To further improve the prediction model performance, some researchers have developed hybrid models of signal decomposition and neural networks to forecast wave parameters. For example, empirical wavelet transform (EWT) (Karbasi et al., 2022), empirical mode decomposition (EMD) (Zhou et al., 2021; Hao et al., 2022), and singular spectrum analysis (SSA) (Rao et al., 2013). However, EMD and its extended algorithms suffer from mode confounding and sensitivity to noise (Bisoi et al., 2019), and wavelet transforms

40   methods lack adaptivity (Li et al., 2017). Variational mode decomposition (VMD) (Dragomiretskiy and Zosso, 2014) has overcome the disadvantages of EMD and is currently the most effective decomposition technique (Duan et al., 2022). Models combining VMD and neural networks are applied in forecasting various time series data. For example, stock price prediction (Bisoi et al., 2019), air quality index prediction (Wu and Lin, 2019), wind power prediction (Duan et al., 2022), runoff prediction (Zuo et al., 2020), and wave energy prediction (Neshat et al., 2022; Jamei et al., 2022).

45   Recent studies have shown that temporal convolutional networks (TCN) outperform ordinary network models in handling time-series data in several domains, such as flood prediction (Xu et al., 2021), traffic flow prediction (Zhao et al., 2019), and dissolved oxygen prediction (Li et al., 2022a). The TCN cells can significantly capture the short-term local feature information of the sequence data, while the LSTM cells are adept at capturing the long-term dependence of the sequence data. The wave data observed by the buoy contains both short-term features and long-term patterns of wave variability and is very well-suited

50   for forecasting using a hybrid prediction model that includes the advantages of TCN and LSTM cells.

Hyperparameter optimization (HPO) for neural networks is commonly regarded as a black-box problem that avoids neural network problems such as overfitting, underfitting or incorrect learning rate values, which tend to occur in constructing deep learning models. The latest HPO techniques are grid search, stochastic search, and Bayesian optimization (BO), etc. BO provides a better hyperparameter combination in a shorter time compared to traditional grid search methods (Rasmussen, 2004).

55   It is more robust and less probable to be trapped in a local optima problem. Therefore, BO is the most widely used HPO algorithm, which has been applied to wave prediction models based on neural network algorithms (Zhou et al., 2022; Cornejo-Bueno et al., 2018).

Significant wave height (SWH) and average wave period (APD) are essential parameters in calculating wave power (De Assis Tavares et al., 2020; Bento et al., 2021). For example, Hu et al. (2021) used XGBoost and LSTM to forecast wave heights

60   and periods. Based on multi-layer perceptron and decision tree architecture, Luo et al. (2023) realized the prediction of effective wave height, average wave period, and average wave direction. The SWH and APD forecasts need to consider the original characteristics of waves, short-term variability, and long-term dependence. Therefore, in the study, we used wave data from the National Data Buoy Center (NDBC) around the Hawaiian Islands to design a hybrid VMD-TCN-LSTM model to forecast SWH and APD, and the BO algorithm was used to obtain the most optimal hyperparameters for the network model.

65 The remaining sections of this paper are organized as follows. In Section 2, the data and pre-processing are described, and in Section 3, the methodologies employed in the study are presented. In Section 4, the decomposition process of the wave series data, the overall structure of the prediction model and the hyperparameter optimization results are presented. Section 5 discusses the performance differences between the VMD-TCN-LSTM, VMD-LSTM, and LSTM models at various forecasting periods. Finally, Section 6 provides our conclusions.

70 ## 2 Materials

2.1 Data source

Buoy measurements are the most common data source for wave parameter forecasts (Cuadra et al., 2016). The research used buoy data from the NDBC of the National Oceanic and Atmospheric Administration (NOAA) (https://www.ndbc.noaa.gov/). Each buoy provides measurements of SWH, mean wave direction (MWD), wind speed (WSPD), wind direction (WDIR), APD,
75 dominant wave period (DPD), sea level pressure (PRES), gust speed (GST), air temperature (ATMP), and water temperature (WTMP) at a resolution of 10 minutes to 1 hour. The dataset uses 99.00 to replace the missing values, but the resolution is still 1 hour for wave parameters data. Four NDBC buoys located in different directions around the Hawaiian Islands (Fig. 1) were used in the research, The statistics of the geographic location and the water depth parameters of the buoys are shown in Table 1.
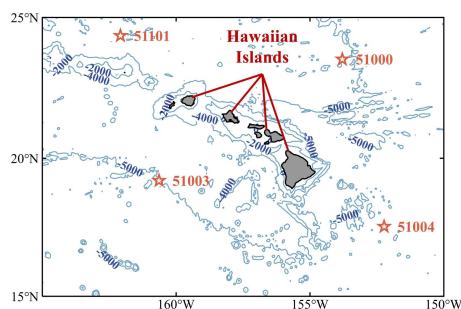
80
Figure 1. The geographical locations of the 51000, 51003, 51004 and 51101 NDBC buoys.

Table 1. Statistics of the geographical locations and water depth parameters of the selected NDBC buoys.

Buoy ID	Latitude (°N)	Longitude (°W)	Depth (m)
51000	23.528	153.792	4762
51003	19.196	160.639	1987
51004	17.538	152.230	5278
51101	24.359	162.081	4860

2.2 Dataset partitioning and feature selection

Waves depend on previous wave height, sea surface temperature, sea temperature, wind direction, wind speed, and pressure
85 (Kamranzad et al., 2011; Nitsure et al., 2012; Fan et al., 2020). Because the buoy data have missing values, after data filtering, the research selected data longer than two years at each buoy as the training datasets to capture the year-round characteristics of wave parameters. The divisions and statistical characteristics of the training and testing datasets for the four buoys are shown in Table 2 and Fig. 2.

Table 2. NDBC datasets division and statistical information.

Buoy ID	Dataset	Date (YYYY/MM/DD HH)	Data volume	SWH range (m)	ADP range (s)
51000	Training	2015/08/20 22~2020/04/20 15	40594	[0.89, 11.03]	[4.60, 14.89]
	Testing	2020/07/29 01~2020/10/19 08	1976	[0.89, 3.49]	[5.12, 11.43]
51003	Training	2015/08/25 03~2018/08/07/13	25494	[0.85, 6.83]	[4.75, 13.85]
	Testing	2018/11/10 00~2018/12/31 08	1214	[1.41, 4.70]	[5.48, 12.79]
51004	Training	2014/07/06 14~2017/10/08 16	28400	[0.86, 5.80]	[4.78, 14.03]
	Testing	2017/12/08 11~2018/02/14 09	1631	[1.29, 5.30]	[5.46, 12.99]
51101	Training	2014/11/04 22~2018/03/29 07	29548	[0.83, 8.54]	[4.46, 14.73]
	Testing	2019/10/25 07~2020/01/04 00	1698	[1.16, 6.04]	[5.44, 13.03]

90
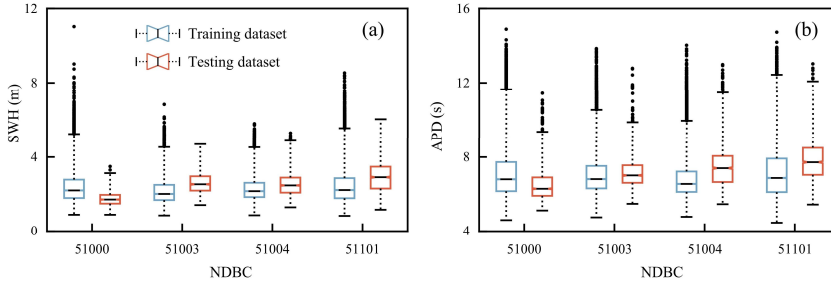
Figure 2. Statistical analysis of SWH and APD on the training and testing datasets of the four NDBC buoys.

The research selected SWH and APD, two wave parameters, as forecasting variables. The correlation between various environmental parameters with SWH and APD was determined by calculating Pearson correlation coefficients between the
95 above parameters before selecting the input features. For the parameters X and Y, the Pearson correlation coefficients are calculated as follows.

$$r = \frac{cov(X, Y)}{\sigma_X \sigma_Y} = \frac{\frac{1}{n}\sum_{i=1}^{n}(X_i - \bar{X})(Y_i - \bar{Y})}{\sqrt{\frac{1}{n}\sum_{i=1}^{n}(X_i - \bar{X})^2}\sqrt{\frac{1}{n}\sum_{i=1}^{n}(Y_i - \bar{Y})^2}}, \qquad (1)$$

The Pearson correlation coefficients between SWH, MWD, WSPD, GST, WDIR, PRES, WTMP, ATMP, APD, and DPD were calculated after neglecting the parameter values at unrecorded moments (Fig. 3). As shown in Fig. 3, SWH has a positive correlation with APD, DPD, MWD, WSPD, GST, WDIR, and PRES to different degrees, and SWH has a negative correlation with WTMP and ATMP. Among them, WSPD and GST have a strong correlation (r=0.988), WTMP and ATMP have a strong correlation (r=0.901), and APD is considered to contain the main features of DPD. In order to utilize as many features of different physical parameters as possible while minimizing the computational redundancy, seven physical parameters, SWH, APD, MWD, WSPD, WDIR, PRES and ATMP, were selected as input and training data for SWH and APD forecasting in the study.
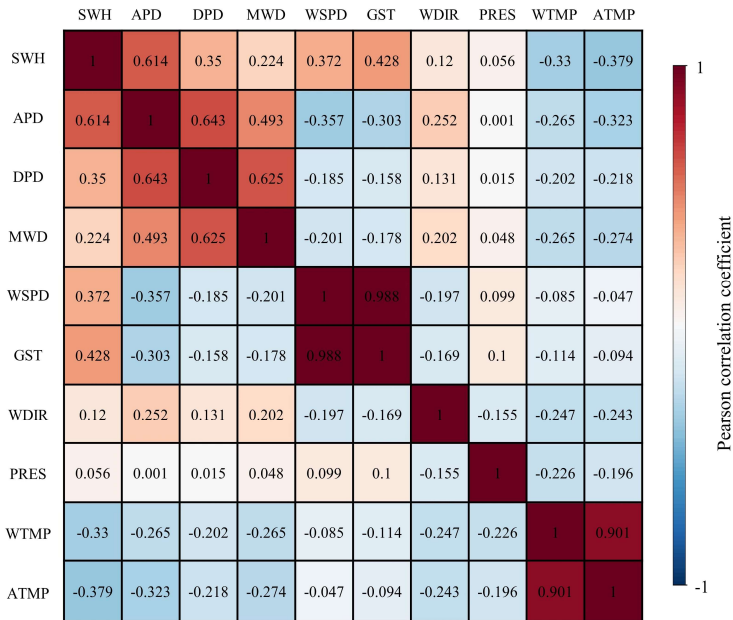
Figure 3. Pearson correlation coefficients between various physical parameters in NDBC data.

2.3 Data pre-processing

Wind and wave directions are continuous in space but discontinuous numerically. For example, the directions 2° and 358° are very close, but the magnitude of the values differs significantly. Therefore, the wind and wave directions need to be pre-processed. The following formula recalculates the wind and wave directions (Nitsure et al., 2012).

$$\psi = \begin{cases} 1 - \frac{\theta}{180}, & if\ 0° \le \theta \le 180° \\ \frac{\theta - 180}{180}, & if\ 180° < \theta < 360° \end{cases},$$ (2)

where θ is the original wind or wave directions and ψ is the re-encoded value of wind or wave directions. ψ has a range of values from [0, 1].

115   Since different NDBC physical variables have different units and magnitudes, this can substantially influence the performance of the neural network model. Therefore, each variable must be normalized or standardized before using it as input data for the model (Li et al., 2022b). The research used a min-max normalization function to scale the input data between [0, 1], which is calculated as follows.

$$x_n = \frac{x - \min(x)}{\max(x) - \min(x)},$$ (3)

120   where x_n is the normalized feature value and x is the measured feature value.

3 Methods

3.1 Variational mode decomposition (VMD)

   The VMD is an adaptive, completely nonrecurrent mode variation and signal processing technique that combines the Wiener filter, the Hilbert transform, and the Alternating Direction Method of Multipliers (ADMM) technique (Dragomiretskiy and

125   Zosso, 2014). VMD can determine the number of mode decompositions for a given sequence according to the situation. It has resolved the issues of mode mixing, boundary effects of EMD. The VMD decomposes the original sequence signal into an Intrinsic Mode Function (IMF) of finite bandwidth, where the frequencies of each mode component u_k are concentrated around a central frequency ω_k. The VMD algorithm can be found in more detail in Appendix A.

~~The nucleus of VMD is the construction and solution of the variational problem, which is essentially a constrained optimization~~

130   ~~problem. The variational problem is to minimize the sum of the estimated bandwidths of the IMFs, with the constraint that the sum of the IMFs is the original signal. The calculation formula is as follows.~~

~~$$\min_{\{u_k\},\{\omega_k\}} \left\{ \sum_k \left\| \partial_t [(\delta(t) + \frac{j}{\pi t}) * u_k(t)] e^{-j\omega_k t} \right\|_2^2 \right\} \quad s.t. \sum_k u_k = f,$$~~ (4)

~~where "s.t." is the abbreviation of "subject to". $\{u_k\} := \{u_1, u_2, ..., u_k\}$ and $\{\omega_k\} := \{\omega_1, \omega_2, ..., \omega_k\}$ denote the set of all modes and their corresponding central frequencies, respectively. The f is the original signal, k is the total number of modes, and $\delta(t)$~~

135   ~~represents the Dirac distribution. The j is an imaginary unit and "*" denotes the convolution.~~

~~To simplify the above equations, VMD introduces a quadratic penalty term (α) and Lagrange multipliers (λ) to convert the constrained problem into a non-constrained problem. α guarantees the reconstruction accuracy of the signal, and λ maintains the constraint stringency.~~

ez

$$\mathcal{L}(\{u_k, \omega_k\}, \lambda) := \alpha \sum_k \left\| \partial_t [(\delta(t) + \frac{j}{\pi t}) * u_k(t)] e^{-j\omega_k t} \right\|_2^2 + \left\| f(t) - \sum_k u_k(t) \right\|_2^2 + \langle \lambda(t), f(t) - \sum_k u_k(t) \rangle, \quad (5)$$

Finally, the ADMM solves the saddle point of the augmented Lagrange multiplier. Update the iterative formulas for u_k, ω_k and λ as follows.

$$\hat{u}_k^{n+1}(\omega) = \frac{\hat{f}(\omega) - \sum_{i \neq k} \hat{u}_i(\omega) + \frac{\hat{\lambda}(\omega)}{2}}{1 + 2\alpha(\omega - \omega_k)^2}, \quad (6)$$

$$\omega_k^{n+1} = \frac{\int_0^\infty \omega |\hat{u}_k(\omega)|^2 d\omega}{\int_0^\infty |\hat{u}_k(\omega)|^2 d\omega}, \quad (7)$$

$$\hat{\lambda}^{n+1}(\omega) = \hat{\lambda}^n(\omega) + \tau(\hat{f}(\omega) - \sum_{k=1}^K \hat{u}_k^{n+1}(\omega)), \quad (8)$$

where $\hat{f}(\omega)$, $\hat{u}_k(\omega)$, $\hat{\lambda}(\omega)$ and $\hat{u}_k^{n+1}(\omega)$ are the Fourier transforms of $f(\omega)$, $u_k(\omega)$, $\lambda(\omega)$ and $u_k^{n+1}(\omega)$, respectively. The n and τ are the number of iterations and update coefficients of Dual ascent. The iterations are stopped when the convergence condition satisfies the following equation.

$$\sum_k \frac{\left\| \hat{u}_k^{n+1} - \hat{u}_k^n \right\|_2^2}{\left\| \hat{u}_k^n \right\|_2^2} < \epsilon, \quad (9)$$

The VMD algorithm can be found in more detail in Dragomiretskiy and Zosso (2014).

3.2 Temporal convolutional networks (TCN)

The TCN is a variant of the Convolutional Neural Networks (CNN) (Fig. 4). TCN model uses causal convolution, dilated convolution, and residual block to extract sequence data with a large receptive field and temporality (Yan et al., 2020). TCN performs convolution in the time domain (Kok et al., 2020), which has a more lightweight network structure than CNN, LSTM, and GRU (Bai et al., 2018). TCN has the following advantages: (1) causal convolution prevents the disclosure of future information, (2) dilated convolution extends the receptive field of the structure, and (3) residual block maintains the historical information for a longer period.

TCN is on the concept of causal convolution, where "causal" indicates that the output y_t (Fig. 4) at the time t is only dependent on the input x_1, $x_2, \ldots, x_t$ and is not influenced by $x_{t+1}, x_{t+2}, \ldots, x_T$. The receptive field depends on the filter size and the network depth. However, the increase of filter size and network depth brings the risk of gradient disappearance and explosion. To avoid these problems, TCN introduces dilated convolution based on causal convolution (Zhang et al., 2019). The dilated convolution introduces a dilation factor to adjust the receptive field. The processing capability of long sequences depends on the filter size, dilation factor, and network depth. TCN effectively increases the receptive field without additional computational cost by increasing the dilation factor. To ensure training efficiency, TCN introduces multiple residual blocks to accelerate the prediction model. Each residual block comprises two dilated causal convolution layers with the same dilation factor, normalization layer, ReLU activation and dropout layer. The input of each residual block is also added to the output when the input and output channels are different.
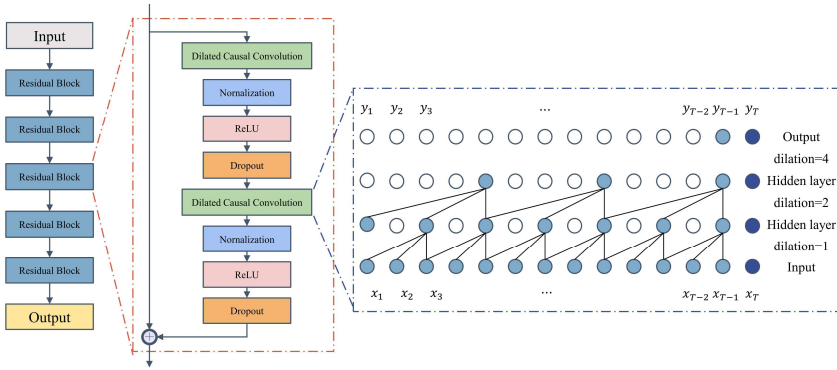
Figure 4. Structure of temporal convolutional networks.

TCN employs dilated convolution based on causal convolution to handle the linear increase in network depth for longer inputs.

170 The dilated convolution introduces a dilation factor (d) to adjust the receptive field. The processing capability of long sequences depends on the filter size (k), d, and network depth (p). For a one-dimensional time series $x \in \mathbb{R}^n$ and a filter f: {0, …, $k -$ 1} → $\mathbb{R}$, the dilated convolution operation F on the sequence element s is defined as:

$$F(s) = (x *_d f)(s) = \sum_{i=0}^{k-1} f(i) \cdot x_{s-d \cdot i}, \tag{10}$$

where d is the dilation factor, k is the filter size, and "$s - d \cdot i$" describes the passed direction. In the dilated convolution, the

175 dilation factor d grows exponentially ($d = 2^i$) with the hidden layer depth (i), and the receptive field is ($k - 1$) d. TCN effectively increases the receptive field without additional computational cost by increasing the dilation factor. Figure 4 illustrates the structural components of TCN with the dilation factors $d = 1, 2,$ and 4.

To ensure training efficiency, TCN introduces multiple residual blocks to accelerate the prediction model. Each residual block comprises two dilated causal convolution layers with the same dilation factor, normalization layer, ReLU activation and

180 dropout layer. The input of each residual block is also added to the output when the input and output channels are different (Fig. 4).

The input of each residual block is also added to the output when the number of channels between the input and output are different (Fig. 4). The following equation obtains the residual block:

$$o = Activation(x + F(x)), \tag{11}$$

185 where o is the residual block output, *Activation* is the activation function, x is the previous input information, and $F(x)$ is the transformed information.

3.3 Long short-term memory (LSTM) networks

The traditional RNN is exposed to gradient explosion and vanishing risk. LSTM network learns to reset itself at the appropriate time by adding a forgetting gate in RNN, which releases internal resources. Meanwhile, LSTM learns faster by adding the self-looping method to generate a long-term continuous flow path. As a specific RNN, the LSTM network structure includes an input layer, a hidden layer, and an output layer. The structure of the LSTM cell is shown in Fig. 5. The LSTM can be found in more detail in Appendix B.
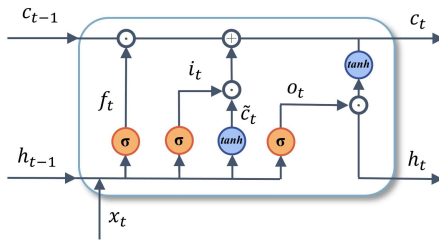
Figure 5. Structure of long short-term memory networks. The x_t denotes the current input vector, f_t is the forget gate, i_t is the input gate, c_t is the storage cell state, o_t is the output gate, h_t is the storage cell value at time t, σ is the sigmoid function, $tanh$ denotes the hyperbolic tangent function, "$\odot$" denotes the Hadamard matrix product.

A LSTM cell consists of four components, the forget gate f_t, the input gate i_t, the storage cell state c_t and the output gate o_t. The f_t determines the number of memories that need to be reserved from c_{t-1} to c_t.

$$f_t = \sigma(W_f \cdot [x_t, h_{t-1}] + b_f),\tag{12}$$

The i_t determines the information that is input to this cell state.

$$i_t = \sigma(W_t \cdot [x_t, h_{t-1}] + b_i),\tag{13}$$

The o_t represents the information output from this cell state.

$$o_t = \sigma(W_o \cdot [x_t, h_{t-1}] + b_o),\tag{14}$$

The cell state is:

$$C_t = f_t \odot C_{t-1} + i_t \odot \tilde{C}_t,\tag{15}$$

$$\tilde{C}_t = \tanh(W_c \cdot [x_t, h_{t-1}] + b_c),\tag{16}$$

The next cell with h_t is:

$$h_t = o_t \odot \tanh(C_t),\tag{17}$$

In the above equation, x_t denotes the current input vector, and W and b denote the hyperparameters of the weights and biases. The h_t is the storage cell value at time t. The σ is the sigmoid function, $tanh$ denotes the hyperbolic tangent function, "$\cdot$" denotes the dot product of matrices, and "$\odot$" denotes the Hadamard matrix product of equidimensional matrices (Yu et al.,

215

3.4 Bayesian optimization (BO)

The BO aims to find the global maximizer (or minimizer) of the unknown objective function $f(x)$ (Frazier, 2018), as shown in follows:

$$x^* = (\arg \max_{x \in D} f(x)) , \tag{18,4}$$

220   where D denotes the search space of x, where each dimension is a hyperparameter.

The BO has two critical components, first, ~~establishing~~build an agency model of the objective function through a regression model (e.g., Gaussian process regression) and subsequently ~~using~~use the acquisition function to decide where to sample next (Frazier, 2018).

The Gaussian process (GP) is an extension of multivariate Gaussian distribution into an infinite dimensional stochastic process
225   (Frazier, 2018; Brochu et al., 2010), which is the prior distribution of stochastic processes and functions. Any finite subset of random variables has a multivariate Gaussian distribution, and a GP is entirely defined by its mean function and covariance function (Rasmussen, 2004). BO optimizes the unknown function $f(x)$ by combining the prior distribution of the function based on the GP with the current sample information to obtain the posterior of the function.

The BO uses the expected improvement (EI) function as the acquisition function to evaluate the utility of the model posterior
230   to determine the next input point. Let f_n^* be the optimal value of the acquisition function at the current iteration. ~~The EI acquisition function can be defined by Eq. (19) (Shahriari et al., 2016; Frazier, 2018):~~

$$EI(x) = \begin{cases} (\mu(x) - f_n^*)\phi(Z) + \sigma(x)\varphi(Z) & if\ \sigma(x) > 0 \\ 0 & if\ \sigma(x) = 0 \end{cases}, \tag{19}$$

235

The BO employs GP and EI in the iterations to evaluate and obtain the global optimal hyperparameters (Zhang et al., 2020a). The framework of the Bayesian parameter optimization algorithm is shown below.

Algorithm 1 Basic pseudo-code for Bayesian optimization
1: Initializing the prior distribution of the substitution function based on GP.
2: **for** $n = 1, 2, \ldots$ **do**
Find x_n by optimizing acquisition function.
$x_{n+1} = \arg \max_x \alpha (x\|D_n)$
Query objective function to obtain y_{n+1}

Augment data $D_{n+1} = \{D_n, \ (x_{n+1}, y_{n+1})\}$
Update the prior distribution of the substitution function.
end for
3: Find the global optimal solution for the current GP.

4 Wave parameter prediction model framework and parameter settings

4.1 Data decomposition and parameter setting

240 The input to the VMD method requires the original signal $f(t)$ and a predefined parameter K. The K determines the number of IMF patterns extracted during the decomposition. If the number of the extracted patterns is too large, it leads to a decrease in accuracy and unnecessary computational overhead (Liu et al., 2020). However, if the number of patterns is too small, the information in the patterns is insufficient to construct a high-precision prediction model. Therefore, it is essential to choose an appropriate one for K.

245 There is still a lack of general guidelines for the selection of the K parameter (Bisoi et al., 2019). Methods commonly used in other fields include the central frequency observation method (Hua et al., 2022; Chen et al., 2022; Fu et al., 2021), sample entropy (Zhang et al., 2020b; Niu et al., 2021), genetic algorithm (Huang et al., 2022), effective kurtosis index (Li et al., 2020), signal energy (Liu et al., 2020; Huang and Deng, 2021), etc. The central frequency observation method is convenient and effective, and it is used in this research to determine the number of patterns K for sequence decomposition. For various K

250 parameter values, when the central frequency of the last mode has no significant changing trend, the number of K currently is the optimal number of mode decompositions. ~~The search range of K parameters in the research is [5, 15], and~~ Table 3 calculates the central frequency of the last mode after the SWH and APD were decomposed with different K parameters~~.~~, the optimal VMD decomposition mode number for SWH and APD is 13 and 12, respectively, when the variation of the central frequency is less than 1e-8 Hz. ~~As shown in Table 3, after VMD decomposes SWH, the central frequency of the last mode from $K = 13$~~

255 ~~does not change significantly, so the optimal VMD decomposition mode number for SWH is 13. As shown in Table 3, after VMD decomposes APD, the central frequency of the last mode from $K = 12$ does not change significantly, so the optimal VMD decomposition mode number for APD is 12. According to the optimal K parameters of SWH and APD decomposition, the SWH and APD data on the training and test sets of each buoy are decomposed by VMD separately.~~

260 **Table 3. The central frequency of the last mode after SWH and APD decomposition with different K parameters.**

K	5	6	7	8	9	10	11	12	13	14	15
last mode after the SWH were decomposed ($\times$ (1e – 6) Hz)	395975	419471	447343	449966	452286	452888	453510	453650	476397	477347	477403

| last mode after the APD were decomposed (× (1e − 6) Hz) | 394750 | 433368 | 433725 | 434455 | 451044 | 451505 | 451713 | 475568 | 476213 | 476246 | 476317 |

4.2 Wave parameter prediction model framework

The overall structure of the VMD-TCN-LSTM wave parameter prediction model in the research is shown in Fig. 6, including three parts: data pre-processing, VMD data decomposition, and model training and forecasting. The input parameters to the model includes 13 SWH IMFs and residual, 12 APD IMFs and residual, original MWD, WSPD, PRES and ATMP, recoded WDIR. The lags of each input variable chosen for prediction are 3 hours. The TCN cells and LSTM cells are used in the model to construct an encoder-decoder network with an attention mechanism. To evaluate the accuracy of the VMD-TCN-LSTM model. The effect of the VMD technique and TCN cells on the forecasting results was also analysed. The results of the VMD-TCN-LSTM model were compared with the VMD-LSTM and LSTM models. The VMD-LSTM model used both LSTM cells for encoding and decoding. The LSTM model without the VMD technique for data decomposition and was not encoded using TCN cells.
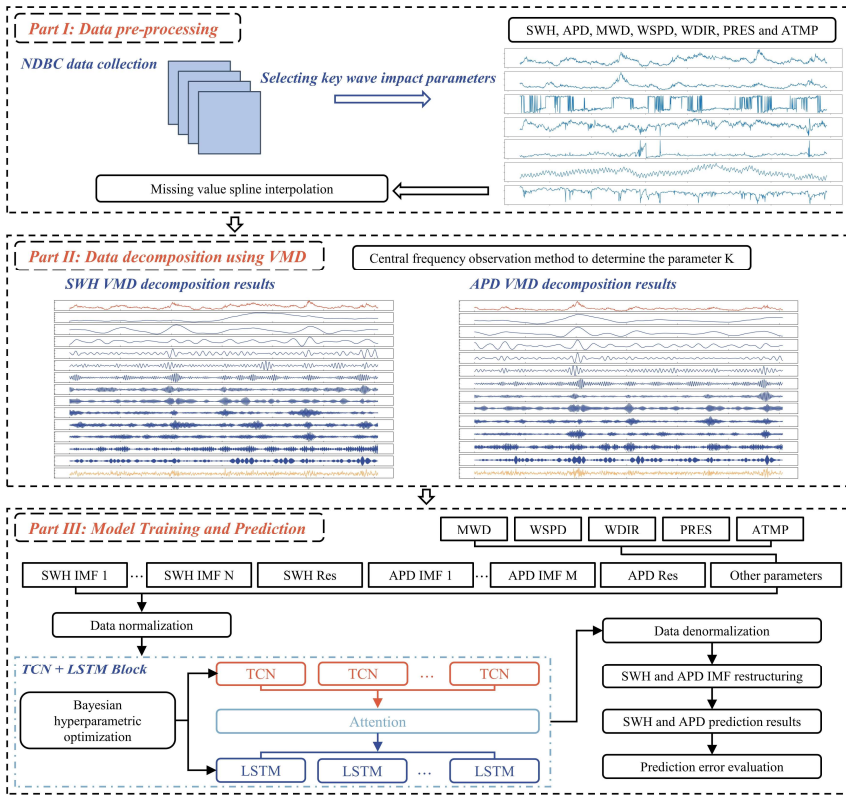
Figure 6. The overall structure of VMD-TCN-LSTM wave parameter prediction model.

4.3 Neural network hyperparameter optimization based on BO

275 In the research, the BO algorithm is used to search for the optimal hyperparameters for the training of the VMD-TCN-LSTM
model, including batch size, number of TCN hidden layer units, number of LSTM hidden layer units, number of Dense hidden
layer units, learning rate (α), dropout rate, and L2 regularization parameter of LSTM layer. The hyperparameters search range
and optimal results are shown in Table 4. Meanwhile, the learning rate decay and Early Stopping method are used to prevent
overfitting of the model and reduce the wasted training time.

280

Table 4. Bayesian hyperparameter optimization results.

Parameter	Search interval	Final value
Batch size	{8, 16, 32, 64, 256, 512}[8, 512]	256
TCN hidden unit	[16, 256]{16, 32, 64, 256}	64
LSTM hidden unit	[16, 256]{16, 32, 64, 256}	128
Dense hidden unit	[16, 256]{16, 32, 64, 256}	128
learning rate α	{[1e-4, 3e-4, 5e-4, 1e-3, 1e-2]}	3e-4
Dropout rate	{0.1, 0.2, 0.3, 0.4, 0.5}[0.1, 0.5]	0.2
L2 regularization parameter	{[1e-7, 1e-6, 1e-5, 1e-4]}	1e-5

5 Experiment and analysis

5.1 Evaluation metrics

To quantify the performance of the prediction model ~~performance~~, the mean absolute error (MAE), root mean square error (RMSE), mean absolute percentage error (MAPE) and the determination coefficient (R^2) are used as evaluation metrics. The equations can be written as follows.

$$MAE = \frac{1}{N}\sum_{i=1}^{N}\left|y_{p(i)} - y_{t(i)}\right|, \tag{205}$$

$$RMSE = \sqrt{\frac{1}{N}\sum_{i=1}^{N}\left(y_{p(i)} - y_{t(i)}\right)^2}, \tag{216}$$

$$MAPE = \frac{1}{N}\sum_{i=1}^{N}\frac{\left|y_{p(i)} - y_{t(i)}\right|}{y_{t(i)}} \times 100\%, \tag{227}$$

$$R^2 = 1 - \frac{\sum_{i=1}^{N}\left(y_{p(i)} - y_{t(i)}\right)^2}{\sum_{i=1}^{N}\left(y_{t(i)} - \bar{y}_t\right)^2}, \tag{238}$$

where N denotes the time length of the series data, $y_{t(i)}$ is the true observation values of NDBC, $y_{p(i)}$ is the predicted value, and $\bar{y}_t$ is the average of the true observation values.

Furthermore, to quantify the improvement of the VMD technique and the TCN unit on the model accuracy, respectively, four parameters, I_{MAE}, I_{RMSE}, I_{MAPE} and I_{R^2} (Eqs. (9) ~~(24)~~ to (12)~~(27)~~), are introduced to compare the percentage improvement of the evaluation metrics of VMD-LSTM and VMD-TCN-LSTM models concerning the LSTM model.

$$I_{MAE} = \frac{MAE_{LSTM} - MAE_{model}}{MAE_{LSTM}} \times 100\%, \tag{249}$$

$$I_{RMSE} = \frac{RMSE_{LSTM} - RMSE_{model}}{RMSE_{LSTM}} \times 100\%, \tag{2510}$$

$$I_{MAPE} = \frac{MAPE_{LSTM} - MAPE_{model}}{MAPE_{LSTM}} \times 100\%, \tag{2611}$$

$$I_{R^2} = \frac{R^2_{model} - R^2_{LSTM}}{R^2_{LSTM}} \times 100\%, \tag{2712}$$

where the subscript "*LSTM*" represents the evaluation metrics of the LSTM model, and the subscript "*model*" represents the evaluation metrics of the VMD-LSTM or VMD-TCN-LSTM models.

5.2 3-hour forecasting performance

The evaluation metrics of SWH and APD for different prediction models on the testing sets of the four buoys for the 3-hour forecasts are shown in Table 5, where the best results are shown in bold. As shown in the table, both the VMD-LSTM and VMD-TCN-LSTM models significantly outperform the results of the LSTM model. This indicates that the data pre-processing method of VMD can extract the features of the sequence data well forin the 3-hour SWH and APD forecasts, which can significantly improve the forecasting performance. Meanwhile, the improvement of the TCN cells on the model performance is not particularly significant in for the 3-hour SWH and APD forecasts. The performance of the VMD-TCN-LSTM model was slightly better than that of the VMD-LSTM model only in some instances.

Table 5. Accuracy evaluation of the three models in 3-hour SWH and APD forecasts.

Buoy ID	Algorithm	SWH				APD			
		MAE (m)	RMSE (m)	MAPE (%)	R^2	MAE (s)	RMSE (s)	MAPE (%)	R^2
51000	VMD+TCN+LSTM	**0.083**	**0.111**	**4.675**	**0.924**	**0.155**	**0.204**	**2.353**	**0.950**
	VMD+LSTM	0.085	0.118	4.766	0.918	0.168	0.217	2.536	0.942
	LSTM	0.143	0.177	8.527	0.874	0.219	0.290	3.295	0.897
51003	VMD+TCN+LSTM	**0.066**	**0.082**	**2.315**	**0.978**	**0.105**	**0.145**	**1.438**	0.973
	VMD+LSTM	0.067	0.088	2.592	0.976	0.108	0.147	1.479	**0.976**
	LSTM	0.153	0.204	5.862	0.869	0.252	0.353	3.397	0.859
51004	VMD+TCN+LSTM	**0.080**	**0.105**	**2.816**	**0.973**	**0.115**	**0.158**	**1.323**	**0.981**
	VMD+LSTM	0.081	0.107	2.856	0.970	0.124	0.164	1.372	0.976
	LSTM	0.159	0.217	6.105	0.885	0.279	0.393	3.601	0.884
51101	VMD+TCN+LSTM	**0.093**	**0.124**	**4.720**	0.952	0.171	0.222	**2.526**	**0.953**
	VMD+LSTM	0.096	0.127	4.795	**0.957**	**0.166**	**0.218**	2.527	0.951
	LSTM	0.224	0.302	7.417	0.892	0.326	0.479	4.269	0.848

In the SWH forecasting at four buoys, the buoy with the best performances was buoy 51003 with MAE, RMSE, MAPE and R^2 of 0.066 m, 0.082 m, 2.315 %, and 0.978, respectively. Among the APD forecasting at four buoys, the VMD-TCN-LSTM model had the most petite MAE and RMSE at buoy 51003, with 0.105 s and 0.145 s, respectively, and the smallest MAPE and the highest R^2 at buoy 51004 with 1.323 % and 0.981, respectively.

To compare the forecasting results of different models more visually, Figure 7 shows the comparison results of the 3-hour SWH and APD forecasting curves of different models with the observed values for the first 24 hours of the testing set for each buoy. As shown in Fig. 7, the forecasting results of VMD-TCN-LSTM have a good agreement with the observed values of

NDBC at most moments on all four buoys. The forecasting results of VMD-LSTM are also close to the observed values. Meanwhile, the results of both the VMD-TCN-LSTM and VMD-LSTM models are significantly better than those of the LSTM model. It shows that both VMD-TCN-LSTM and VMD-LSTM models can better capture the time-varying characteristics of wave series data and thus perform well in the SWH and APD forecasts.

320
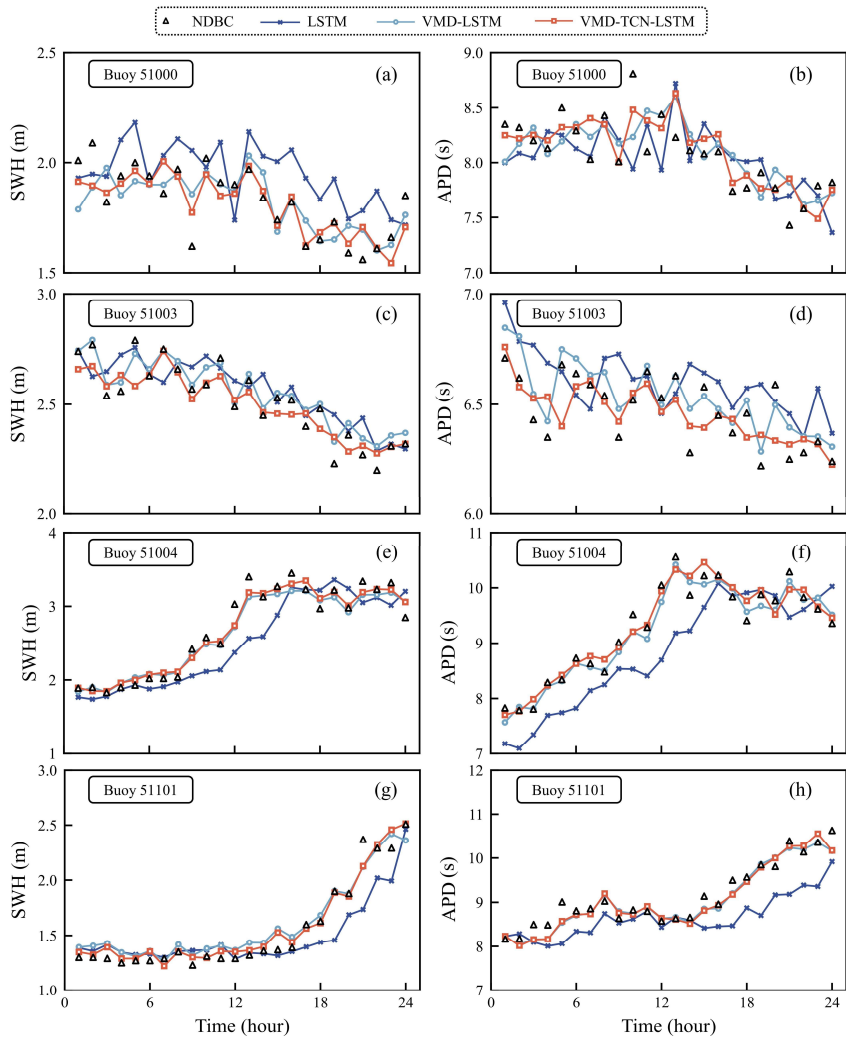
Figure 7. Comparison results of the 3-hour SWH and APD forecasting curves of different models with the observed values for the first 24 hours of the testing datasets for each buoy.

Figure 8 shows the linear fitting results of the SWH and APD observations with the forecasts of the three models for each buoy. According to the linear fitting formula, the fitting curves of both the VMD-LSTM and VMD-TCN-LSTM models were closer to "$y = x$" compared to the LSTM model. For the 3-hour SWH forecasts, the fitted formula of the VMD-TCN-LSTM forecasting results for buoy 51004 was closest to "$y = x$", which had a slope of 0.9817 and an intercept of 0.0404 (Fig. 8(e)).

330 For the 3-hour APD forecasts, the fitted formula of the VMD-TCN-LSTM forecasting results for buoy 51004 was closest to "$y = x$", which had a slope of 0.9929 and an intercept of 0.0829 (Fig. 8(f)). The results indicate that the forecasting performance of these two models is significantly better than that of the LSTM model, which is consistent with the findings in Fig. 7 and Table 5.
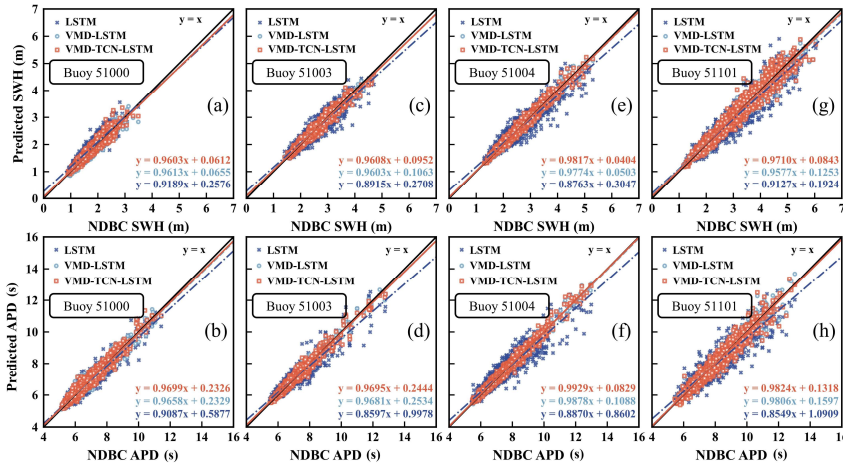
335 **Figure 8. The linear fitting of the 3-hour SWH and APD predictions and observations for the three models.**

Meanwhile, the SWH and APD of the four buoys have different ranges of values and other statistical features, which proves that the two models, VMD-LSTM and VMD-TCN-LSTM, have good robustness for SWH and APD forecasting under different scenarios. The VMD technique can extract the time-varying features of the original data, contributing to the accuracy of the prediction model. In addition, using TCN cells instead of LSTM cells for encoding the network model can also reduce the

340 error of the prediction model by a small amount.

5.3 12-hour forecasting performance

The evaluation metrics of SWH and APD for different prediction models on the testing sets of the four buoys for the 12-hour forecasts are shown in Table 6, and the best results are shown in bold in the table. As shown in Table 6, both the VMD-LSTM

and VMD-TCN-LSTM models significantly outperform the performances of the LSTM model. This is like the results of the
345 3-hour SWH and APD forecasts.

In addition, the performances of the VMD-TCN-LSTM model outperformed the VMD-LSTM for the SWH and APD forecasts
at all buoys. Compared with the 3-hour forecasts, the TCN cells were more significant for the model performance improvement
in the 12-hour wave forecasts. This is because the residual block structure used in the TCN cells can maintain the historical
information for a long time. The TCN cells are more significant in the longer time wave parameter forecasts.

350 Among the SWH forecasting of the four buoys, the VMD-TCN-LSTM model had the smallest MAE and RMSE at buoy 51000
with 0.125 m and 0.165 m, respectively. Buoy 51003 had the smallest MAPE of 5.912 %. Buoy 51004 had the largest R^2 of
0.898. In the APD forecasting at four buoys, the VMD-TCN-LSTM model had the most petite MAE and RMSE at buoy 51003,
with 0.247 s and 0.336 s, respectively, and the smallest MAPE and the highest R^2 at buoy 51004 with 3.329 % and 0.904,
respectively.

355 The comparison of the forecasting curves of different models with the observations of NDBC for the first 24 hours of the
testing set of the four NDBC buoys for the 12-hour SWH and APD forecasts is shown in Fig. 9. As shown in the figure, the
forecasts of the VMD-TCN-LSTM model were in excellent agreement with the NDBC observations for most moments at all
four buoys. And it is significantly outperforming the forecasting curves of VMD-LSTM and LSTM models. The results show
that the VMD-TCN-LSTM model can better capture the time-varying characteristics of wave series data and thus performs
360 well in forecasting SWH and APD.

Table 6. Accuracy evaluation of the three models in 12-hour SWH and APD forecasts.

Buoy ID	Algorithm	SWH				APD			
		MAE (m)	RMSE (m)	MAPE (%)	R^2	MAE (s)	RMSE (s)	MAPE (%)	R^2
51000	VMD+TCN+LSTM	**0.125**	**0.165**	**7.128**	**0.817**	**0.282**	**0.382**	**4.212**	**0.834**
	VMD+LSTM	0.136	0.182	7.706	0.772	0.302	0.406	4.520	0.801
	LSTM	0.195	0.248	11.62	0.639	0.353	0.485	5.210	0.710
51003	VMD+TCN+LSTM	**0.152**	**0.203**	**5.912**	**0.872**	**0.247**	**0.336**	**3.355**	**0.871**
	VMD+LSTM	0.177	0.233	6.910	0.830	0.293	0.398	3.948	0.819
	LSTM	0.271	0.371	10.39	0.581	0.439	0.629	5.862	0.550
51004	VMD+TCN+LSTM	**0.157**	**0.206**	**6.167**	**0.898**	**0.259**	**0.361**	**3.329**	**0.904**
	VMD+LSTM	0.169	0.222	6.575	0.882	0.291	0.395	3.799	0.884
	LSTM	0.277	0.398	10.65	0.619	0.506	0.743	6.457	0.581
51101	VMD+TCN+LSTM	0.283	0.369	9.575	0.839	**0.419**	**0.555**	**5.262**	**0.811**
	VMD+LSTM	**0.274**	**0.361**	**9.270**	**0.840**	0.441	0.585	5.526	0.787
	LSTM	0.384	0.522	12.98	0.673	0.638	0.918	7.876	0.450

设置了格式: 字体: 非加粗

设置了格式: 字体: 加粗
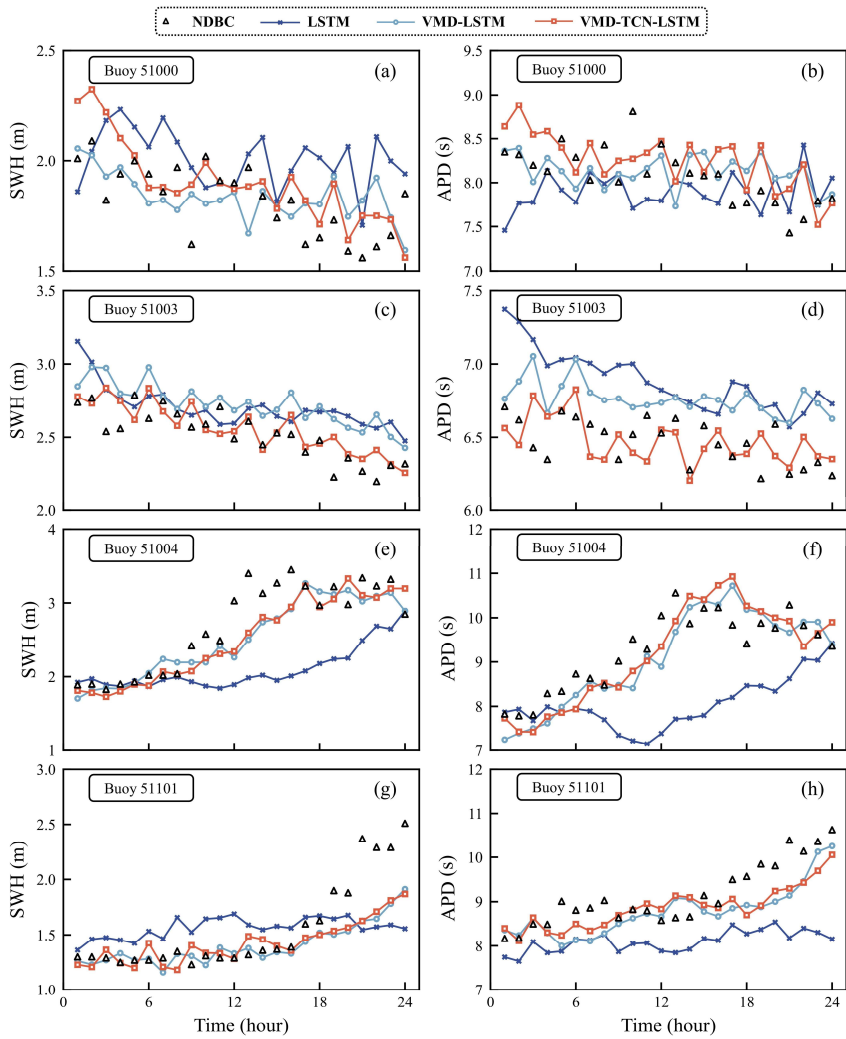
Figure 9. Comparison results of the 12-hour SWH and APD forecasting curves of different models with the observed values for the first 24 hours of the testing datasets for each buoy.

Figure 10 shows the linear fitting results for the 12-hour SWH and APD forecasts data and observations at each buoy for the three models. As shown in Fig. 10, it was evident that the forecasting results of the VMD-TCN-LSTM model have the closest fitting formula to "$y = x$" compared with the LSTM model, and the VMD-TCN-LSTM model is better than the VMD-LSTM model. In the 12-hour SWH forecasts, the fitted formula of the VMD-TCN-LSTM forecasting results for buoy 51000 was closest to "$y = x$", which had a slope of 0.9256 and an intercept of 0.1252 (Fig. 10(a)). Among the 12-hour APD forecasts, the fitted formula of the VMD-TCN-LSTM forecasting results for buoy 51004 was closest to "$y = x$", which had a slope of 0.9664 and an intercept of 0.2500 (Fig. 10(f)). Both VMD-TCN-LSTM and VMD-LSTM models have significantly better forecasting performance than the LSTM model. This is consistent with the conclusions of Fig. 9 and Table 6.
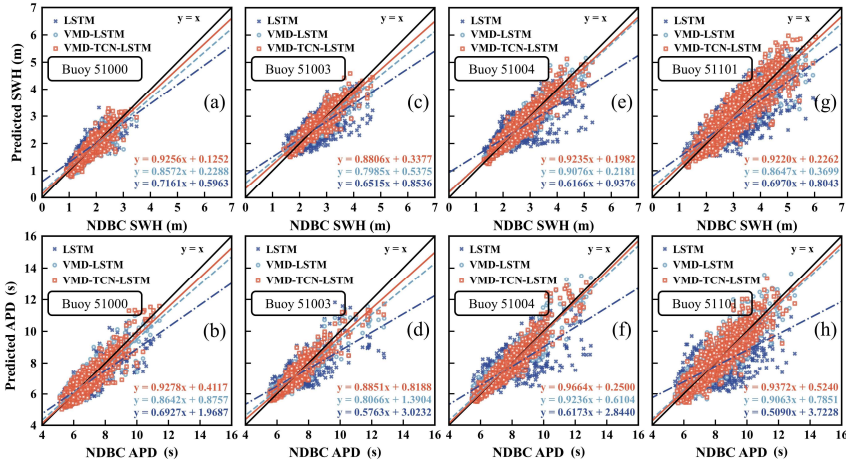
Figure 10. The linear fitting of the 12-hour SWH and APD predictions and observations for the three models.

Moreover, the variability of the numerical ranges of SWH and APD for the four buoys also demonstrates the excellent robustness of the VMD-TCN-LSTM model for SWH and APD forecasts in different scenarios. The pre-processing of wave sequence data using VMD can extract the time-varying features of the original data well, and the expansion convolution module of TCN increases the perceptual field of the model. At the same time, the residual block enables the preservation of the long-term information of the original data. Therefore, the hybrid model of VMD, TCN, and LSTM can significantly improve the accuracy of the forecasting results.

5.4 24-, and 48-hour forecasting performance

To further compare the performance of the VMD-TCN-LSTM model for the longer time wave forecasts, the error indices of the prediction models at 24 and 48 hours are presented in Table 7 and Table 8, respectively, where the best results are shown 385 in bold in the table.

Table 7. Accuracy evaluation of the three models in 24-hour SWH and APD forecasts.

Buoy ID	Algorithm	SWH				APD			
		MAE (m)	RMSE (m)	MAPE (%)	R^2	MAE (s)	RMSE (s)	MAPE (%)	R^2
51000	VMD+TCN+LSTM	**0.119**	**0.173**	**8.203**	**0.733**	**0.302**	**0.412**	**4.287**	**0.775**
	VMD+LSTM	0.149	0.206	8.406	0.693	0.336	0.459	4.976	0.739
	LSTM	0.249	0.313	14.87	0.294	0.464	0.648	6.841	0.478
51003	VMD+TCN+LSTM	**0.194**	**0.247**	**7.604**	**0.808**	**0.312**	**0.420**	**4.268**	**0.810**
	VMD+LSTM	0.233	0.290	9.152	0.734	0.342	0.457	4.705	0.764
	LSTM	0.381	0.503	14.44	0.302	0.585	0.842	7.777	0.298
51004	VMD+TCN+LSTM	**0.191**	**0.253**	**7.408**	**0.845**	**0.337**	**0.467**	**4.266**	**0.833**
	VMD+LSTM	0.213	0.282	8.302	0.808	0.405	0.555	5.297	0.764
	LSTM	0.362	0.519	14.29	0.349	0.693	0.959	8.941	0.295
51101	VMD+TCN+LSTM	**0.309**	**0.400**	**10.75**	**0.803**	**0.496**	**0.671**	**6.258**	**0.688**
	VMD+LSTM	0.325	0.416	11.49	0.787	0.517	0.701	6.497	0.659
	LSTM	0.578	0.780	18.81	0.247	0.847	1.169	10.43	0.257

Table 8. Accuracy evaluation of the three models in 48-hour SWH and APD forecasts.

Buoy ID	Algorithm	SWH				APD			
		MAE (m)	RMSE (m)	MAPE (%)	R^2	MAE (s)	RMSE (s)	MAPE (%)	R^2
51000	VMD+TCN+LSTM	**0.187**	**0.249**	**10.64**	**0.551**	**0.443**	**0.604**	**6.676**	**0.487**
	VMD+LSTM	0.197	0.261	10.87	0.505	0.476	0.656	6.899	0.432
	LSTM	0.312	0.390	19.06	0.204	0.602	0.798	8.851	0.160
51003	VMD+TCN+LSTM	**0.315**	**0.387**	**12.56**	**0.536**	**0.448**	**0.606**	**6.174**	**0.592**
	VMD+LSTM	0.335	0.428	13.51	0.434	0.531	0.792	7.110	0.429
	LSTM	0.552	0.720	19.85	0.214	0.772	1.097	10.41	0.214
51004	VMD+TCN+LSTM	**0.255**	**0.339**	**9.879**	**0.723**	**0.524**	**0.715**	**6.714**	**0.611**
	VMD+LSTM	0.299	0.389	11.78	0.635	0.564	0.787	7.247	0.529
	LSTM	0.469	0.644	18.71	0.231	0.859	1.243	11.08	0.276
51101	VMD+TCN+LSTM	**0.456**	**0.586**	**16.23**	**0.580**	**0.744**	**0.907**	**9.474**	**0.432**
	VMD+LSTM	0.497	0.648	16.74	0.487	0.822	1.109	10.31	0.390
	LSTM	0.651	0.805	23.86	0.238	1.127	1.503	13.65	0.180

As shown in Table 7, for the 24-hour forecasts, the MAE and RMSE for the forecasting of SWH and APD at buoy 51000 are
the minimum, with MAE of 0.119 m and 0.302 s, and RMSE of 0.173 m and 0.412 s, respectively. This is because the range
of data for SWH and APD in the testing datasets at buoy 51000 is the minimum (Fig. 2). At Bbuoy 51004, the forecasting of
SWH and APD had the minimum MAPE and the maximum R^2, with MAPE of 7.408 % and 4.266 %, and R^2 of 0.845 and
0.833, respectively.

As shown in Table 8, for the 48-hour forecasts, the MAE and RMSE for the forecasting of SWH and APD at buoy 51000 are
the minimum, with MAE of 0.187 m and 0.443 s and RMSE of 0.249 m and 0.604 s, respectively. It showed a similar
performance as the 24-hour SWH and APD forecasts. Buoy 51004 had the maximum R^2 with 0.723 and 0.611 for SWH and
APD forecasts, respectively. Buoy 51004 also had a minimum MAPE of 9.879 % for the SWH forecasts. Buoy 51003 had a
minimum MAPE of 6.174 % for the APD forecasts.

5.5 Analysis of improvement of VMD-TCN-LSTM compared with previous models

To precisely quantify the prediction performance improvement rate of the VMD technique and TCN cells for the LSTM model,
respectively. The model performance improvement rates for VMD-TCN-LSTM and VMD-LSTM were calculated by using
Eqs. (9)(24) to (12) (27) (Table 9), and bold in the table represents the highest result of the model performance improvement
rate. As shown in Table 9, VMD-LSTM and VMD-TCN-LSTM models had very similar improvement rates in MAE, RMSE,
MAPE, and R^2 in the 3-hour SWH forecasts, which indicates that the improvement of the VMD-TCN-LSTM model for
prediction accuracy in the 3-hour SWH forecasts is mainly contributed by the VMD technique. The same conclusion can be
obtained in the 3-hour APD forecasts. Subsequently, when the length of forecasting increases to 12, 24, and 48 hours, the TCN
cells asis more significant for the decrease of MAE, RMSE, MAPE, and the increase of R^2 for the forecasting results.

Table 9. The performance improvement rate of VMD-TCN-LSTM and VMD-LSTM models relative to LSTM model.

Evaluation indicators	Algorithm	SWH				APD			
		3-hour	12-hour	24-hour	48-hour	3-hour	12-hour	24-hour	48-hour
I_{MAE} (%)	VMD+TCN+LSTM	**51.75**	**37.36**	**48.77**	**39.65**	**48.47**	**36.75**	**43.60**	**35.34**
	VMD+LSTM	50.74	33.14	40.98	34.02	46.27	30.27	37.41	28.39
I_{RMSE} (%)	VMD+TCN+LSTM	**51.91**	**39.08**	**48.90**	**39.24**	**50.51**	**39.69**	**45.11**	**37.80**
	VMD+LSTM	49.71	34.72	42.22	33.18	49.07	34.03	39.26	27.12
I_{MAPE} (%)	VMD+TCN+LSTM	**48.98**	**37.52**	**45.80**	**40.02**	**47.59**	**35.89**	**43.69**	**33.82**
	VMD+LSTM	47.12	33.51	40.23	35.45	45.55	29.22	36.31	28.20
I_{R^2} (%)	VMD+TCN+LSTM	**8.733**	**36.92**	**171.0**	**169.3**	**10.63**	**52.91**	**146.0**	**160.6**
	VMD+LSTM	8.560	32.74	157.2	132.5	10.30	47.19	131.6	119.7

There was no significant rule for the decreased rate of TCN cells on the MAE, RMSE, and MAPE of the model at various
forecasting time length. However, the contribution of TCN cells to the improvement of R^2 for forecasting results gradually

increases with the increase of forecasting time length. It reaches the maximum value in the 48-hour SWH and APD forecasts. As shown in Table 9, in the 48-hour SWH forecasts, the VMD technique increases the R^2 of the forecasting performance by 132.5 %, and the TCN cells for model encoding resulted in a further 36.8 % improvement in the R^2 of the model. In the 48-hour APD forecasts, the VMD technique increases the R^2 of the forecasting performance by 119.7 %. The TCN cells resulted in a further 40.9 % improvement in the R^2 of the model.

LSTM has advantages in solving the prediction problem by using time series data, and has been widely used in many fields. However, due to the strong nonlinear effects in the generation and evolution of wave, the wave prediction model that only uses LSTM will weak in the ability of generalization. As a result, both the model's ability to adapt to new samples and its prediction accuracy will be reduced. The VMD signal decomposition method can effectively extract the features of the original wave data, which can enhance LSTM's ability to capture the long-term dependence of the time series data and further improve the performance of the wave prediction model. This study shows that the VDM can significantly reduce the model's MAE, RMSE and MAPE and improve the model's R^2. TCN introduces multiple residual blocks to speed up the forecast model and can retain historical wave change information over long periods. This study also shows that TCN's impact increases as the forecast period lengthens. The proposed hybrid VMD-TCN-LSTM shows its advantage in predicting both the wave height and the wave period. This method could also be used in other fields which have similar nonlinear features as waves.

6 Conclusions

This paper proposes a hybrid VMD-TCN-LSTM model for forecasting SWH and APD using buoy data near the Hawaiian Islands provided by the NDBC. Seven physical parameters, SWH, APD, MWD, WSPD, WDIR, PRES, and ATMP, were chosen for training the prediction model in the research. Specifically, the original features of the non-smooth wave series data were extracted by decomposing the original SWH and APD series data using the VMD technique. Subsequently, a prediction model is constructed using a network structure encoded by TCN cells and decoded by LSTM cells, where the TCN cells can capture the local feature information of the original series and can maintain the historical information for a long time. Simultaneously, the BO algorithm is used to obtain the optimal hyperparameters of the model to prevent overfitting or underfitting problems of the model. Ultimately, the 3-, 12-, 24-, and 48-hour forecasts of SWH and APD were implemented based on the VMD-TCN-LSTM model. In addition, eight evaluation metrics, MAE, RMSE, MAPE, R^2, I_{MAE}, I_{RMSE}, I_{MAPE}, and I_{R^2}, were used to evaluate and test the model performance.

The VMD-TCN-LSTM model proposed in this research outperforms the LSTM and the VMD-LSTM models for all forecasting time lengths at all four NDBC buoys. It demonstrates that the VMD-TCN-LSTM model has good robustness and generalization ability. For~~In~~ the 3-hour SWH and APD forecasts, the improvement of the hybrid model for forecasting accuracy is mainly contributed by the VMD technique, and the contribution of the TCN cells to the advancement of the model accuracy

is relatively tiny. Subsequently, the contribution of TCN cells to improve model forecasting accuracy was gradually significant when the forecasting time length increased to 12, 24, and 48 hours.

There was no significant rule for the decreased rate of TCN cells on the MAE, RMSE, and MAPE of the model at various forecasting time lengths. The contribution of TCN cells to improving R^2 for forecasting results gradually increases with the increase of forecasting time length. The VMD technique and the TCN cells improved the R^2 of the model by 132.5 % and 36.8 %, respectively, in the 48-hour SWH forecasts. In the 48-hour APD forecasts, the VMD technique and the TCN cells improved the R^2 of the model by 119.7 % and 40.9 %, respectively.

Now that the short term SWH and APD can be accurately predicted using the hybrid VMD-TCN-LSTM, this method would be useful for some marine related activities which are highly dependent on wave height and period predictions, such as ocean wave energy projects, shipping, fishing, coastal structures, and naval operations. Future work will investigate the effect of different driving data on the prediction skill, or the use of VMD-TCN-LSTM to predict other marine environmental parameters (e.g., sea level or winds). The combination of numerical wave models and the VMD-TCN-LSTM for large-scale SWH and APD simulations will also be developed.

Appendix A: Detailed description of the VMD algorithm

The nucleus of VMD is the construction and solution of the variational problem, which is essentially a constrained optimization problem. The variational problem is to minimize the sum of the estimated bandwidths of the IMFs, with the constraint that the sum of the IMFs is the original signal. The calculation formula is as follows:

$$\min_{\{u_k\},\{\omega_k\}} \left\{ \sum_k \left\| \partial_t \left[\left(\delta(t) + \frac{j}{\pi t} \right) * u_k(t) \right] e^{-j\omega_k t} \right\|_2^2 \right\} \quad s.t. \sum_k u_k = f, \tag{A1}$$

where "$s.t.$" is the abbreviation of "subject to". $\{u_k\} := \{u_1, u_2, \ldots, u_k\}$ and $\{\omega_k\} := \{\omega_1, \omega_2, \ldots, \omega_k\}$ denote the set of all modes and their corresponding central frequencies, respectively. The f is the original signal, k is the total number of modes, and $\delta(t)$ represents the Dirac distribution. The j is an imaginary unit and "$*$" denotes the convolution.

To simplify the above equations, VMD introduces a quadratic penalty term (α) and Lagrange multipliers (λ) to convert the constrained problem into a non-constrained problem. α guarantees the reconstruction accuracy of the signal, and λ maintains the constraint stringency.

$$\mathcal{L}(\{u_k, \omega_k\}, \lambda) := \alpha \sum_k \left\| \partial_t \left[\left(\delta(t) + \frac{j}{\pi t} \right) * u_k(t) \right] e^{-j\omega_k t} \right\|_2^2 + \left\| f(t) - \sum_k u_k(t) \right\|_2^2 + \left\langle \lambda(t), f(t) - \sum_k u_k(t) \right\rangle, \tag{A2}$$

Finally, the ADMM solves the saddle point of the augmented Lagrange multiplier. Update the iterative formulas for u_k, ω_k and λ as follows.

$$\hat{u}_k^{n+1}(\omega) = \frac{\hat{f}(\omega) - \sum_{i \neq k} \hat{u}_i(\omega) + \frac{\hat{\lambda}(\omega)}{2}}{1 + 2\alpha(\omega - \omega_k)^2}, \tag{A3}$$

$$\omega_k^{n+1} = \frac{\int_0^\infty \omega |\hat{u}_k(\omega)|^2 d\omega}{\int_0^\infty |\hat{u}_k(\omega)|^2 d\omega}, \tag{A4}$$

$$\hat{\lambda}^{n+1}(\omega)=\hat{\lambda}^{n}(\omega) + \tau\left(\hat{f}(\omega) - \sum_{k=1}^{K} \hat{u}_k^{n+1}(\omega)\right), \tag{A5}$$

where $\hat{f}(\omega)$, $\hat{u}_k(\omega)$, $\hat{\lambda}(\omega)$ and $\hat{u}_k^{n+1}(\omega)$ are the Fourier transforms of $f(\omega)$, $u_k(\omega)$, $\lambda(\omega)$ and $u_k^{n+1}(\omega)$, respectively. The n and τ are the number of iterations and update coefficients of Dual ascent. The iterations are stopped when the convergence condition satisfies the following equation.

$$\sum_k \frac{\left\| \hat{u}_k^{n+1} - \hat{u}_k^n \right\|_2^2}{\left\| \hat{u}_k^n \right\|_2^2} < \epsilon, \tag{A6}$$

Appendix B: Detailed description of the LSTM

A LSTM cell consists of four components, the forget gate f_t, the input gate i_t, the storage cell state c_t and the output gate o_t. The f_t determines the number of memories that need to be reserved from c_{t-1} to c_t.

$$f_t = \sigma(W_f \cdot [x_t, h_{t-1}] + b_f), \tag{B1}$$

The i_t determines the information that is input to this cell state.

$$i_t = \sigma(W_i \cdot [x_t, h_{t-1}] + b_i), \tag{B2}$$

The o_t represents the information output from this cell state.

$$o_t = \sigma(W_o \cdot [x_t, h_{t-1}] + b_o), \tag{B3}$$

The cell state is:

$$C_t = f_t \odot C_{t-1} + i_t \odot \widetilde{C}_t, \tag{B4}$$

$$\widetilde{C}_t = \tanh(W_c \cdot [x_t, h_{t-1}] + b_c), \tag{B5}$$

The next cell with h_t is:

$$h_t = o_t \odot \tanh(C_t), \tag{B6}$$

In the above equation, x_t denotes the current input vector, and W and b denote the hyperparameters of the weights and biases. The h_t is the storage cell value at time t. The σ is the sigmoid function, $tanh$ denotes the hyperbolic tangent function, "·" denotes the dot product of matrices, and "$\odot$" denotes the Hadamard matrix product of equidimensional matrices (Yu et al., 2019; Gers et al., 2000; Hochreiter and Schmidhuber, 1997). The sigmoid function takes values in the range is [0, 1], and in the forgetting gate, if the value is 0, the information of the previous state is completely forgotten, and if the value is 1, the information is completely retained. tanh function takes the values in the range [-1, 1].

Data availability

The buoy data can be found in the National Data Buoy Center (https://www.ndbc.noaa.gov/, last access: 5 June 2022).

Author contributions

QJ and LH provided the initial scientific idea, conducted the models' experiments, and wrote the original paper. LJ and YL supervised the work. YZ and MX collected and pre-processed the data sets. All authors reviewed and edited the manuscript to 500 its final version.

Competing interests

The authors declare that they have no conflict of interest.

Acknowledgements

We thank the wave buoy data obtained from the National Data Buoy Center for the case study in this paper. We also thank the 505 Key Laboratory of South China Sea Meteorological Disaster Prevention and Mitigation of Hainan Province, the Basic Scientific Research Business Expenses of Zhejiang Provincial Universities, the Basic Public Welfare Research Project of Zhejiang Province, and the Innovation Group Project of Southern Marine Science and Engineering Guangdong Laboratory (Zhuhai) for funding and supporting this research.

Financial support

510 This research was funded by the Key Laboratory of South China Sea Meteorological Disaster Prevention and Mitigation of Hainan Province (grant no. SCSF202204), the Basic Scientific Research Business Expenses of Zhejiang Provincial Universities (grant no. 2020J00008), the Basic Public Welfare Research Project of Zhejiang Province (grant no. LGF22D060001), and the Innovation Group Project of Southern Marine Science and Engineering Guangdong Laboratory (Zhuhai) (grant no. SML2020SP007 and 311020004).

515 **References**

Bai, S., Kolter, J. Z., and Koltun, V.: An Empirical Evaluation of Generic Convolutional and Recurrent Networks, arXiv, abs/1803.01271, https://doi.org/10.48550/arXiv.1803.01271, 2018.

Bento, P. M. R., Pombo, J. A. N., Mendes, R. P. G., Calado, M. R. A., and Mariano, S. J. P. S.: Ocean wave energy forecasting using optimised deep learning neural networks, Ocean Eng., 219, 108372, 520 https://doi.org/10.1016/j.oceaneng.2020.108372, 2021.

Bisoi, R., Dash, P. K., and Parida, A. K.: Hybrid Variational Mode Decomposition and evolutionary robust kernel extreme learning machine for stock price and movement prediction on daily basis, Appl. Soft Comput., 74, 652–678, https://doi.org/10.1016/j.asoc.2018.11.008, 2019.

Booij, N., Ris, R. C., and Holthuijsen, L. H.: A third-generation wave model for coastal regions: 1. Model description and 525 validation, J. Geophys. Res. Ocean, 104, 7649-7666, https://doi.org/10.1029/98jc02622, 1999.

Bretschneider, C. L.: Hurricane design—Wave practices, J. Waterways Harb. Div., 124, 39–62, 1957.

Brochu, E., Cora, V. M., and Freitas, N. d.: A Tutorial on Bayesian Optimization of Expensive Cost Functions, with Application to Active User Modeling and Hierarchical Reinforcement Learning, arXiv, abs/1012.2599, https://doi.org/10.48550/arXiv.1012.2599, 2010.

530 Chen, X., Ding, K., Zhang, J., Han, W., Liu, Y., Yang, Z., and Weng, S.: Online prediction of ultra-short-term photovoltaic power using chaotic characteristic analysis, improved PSO and KELM, Energy, 248, https://doi.org/10.1016/j.energy.2022.123574, 2022.

Cornejo-Bueno, L., Garrido-Merchán, E. C., Hernández-Lobato, D., and Salcedo-Sanz, S.: Bayesian optimization of a hybrid system for robust ocean wave features prediction, Neurocomputing, 275, 818-828, 535 https://doi.org/10.1016/j.neucom.2017.09.025, 2018.

Cuadra, L., Salcedo-Sanz, S., Nieto-Borge, J. C., Alexandre, E., and Rodríguez, G.: Computational intelligence in wave energy: Comprehensive review and case study, Renew. Sust. Energ. Rev., 58, 1223-1246, https://doi.org/10.1016/j.rser.2015.12.253, 2016.

De Assis Tavares, L. F., Shadman, M., De Freitas Assad, L. P., Silva, C., Landau, L., and Estefen, S. F.: Assessment of the 540 offshore wind technical potential for the Brazilian Southeast and South regions, Energy, 196, https://doi.org/10.1016/j.energy.2020.117097, 2020.

Deo, M. C. and Naidu, C. S.: Real time wave forecasting using neural networks, Ocean Eng., 26, 191-203, https://doi.org/10.1016/S0029-8018(97)10025-7, 1998.

Dragomiretskiy, K. and Zosso, D.: Variational Mode Decomposition, IEEE Trans. Signal Process., 62, 531-544, 545 https://doi.org/10.1109/tsp.2013.2288675, 2014.

Duan, J., Wang, P., Ma, W., Fang, S., and Hou, Z.: A novel hybrid model based on nonlinear weighted combination for short-term wind power forecasting, Int. J. Elec. Power, 134, 107452, https://doi.org/10.1016/j.ijepes.2021.107452, 2022.

Fan, S., Xiao, N., and Dong, S.: A novel model to predict significant wave height based on long short-term memory network, Ocean Eng., 205, 107298, https://doi.org/10.1016/j.oceaneng.2020.107298, 2020.

550 Frazier, P. I.: A tutorial on bayesian optimization, arXiv, abs/1012.2599, 2018.

Fu, W., Fang, P., Wang, K., Li, Z., Xiong, D., and Zhang, K.: Multi-step ahead short-term wind speed forecasting approach coupling variational mode decomposition, improved beetle antennae search algorithm-based synchronous optimization and Volterra series model, Renew. Energ., 179, 1122-1139, https://doi.org/10.1016/j.renene.2021.07.119, 2021.

Gao, S., Huang, J., Li, Y., Liu, G., Bi, F., and Bai, Z.: A forecasting model for wave heights based on a long short-term memory 555 neural network, Acta Oceanol. Sin., 40, 62-69, https://doi.org/10.1007/s13131-020-1680-3, 2021.

Gers, F. A., Schmidhuber, J., and Cummins, F.: Learning to Forget Continual Prediction with LSTM, Neural Comput., 12, 2451–2471, https://doi.org/10.1162/089976600300015015, 2000.

Hao, W., Sun, X., Wang, C., Chen, H., and Huang, L.: A hybrid EMD-LSTM model for non-stationary wave prediction in offshore China, Ocean Eng., 246, 110566, https://doi.org/10.1016/j.oceaneng.2022.110566, 2022.

560 Hochreiter, S. and Schmidhuber, J.: Long Short-Term Memory, Neural Comput., 9, 1735–1780 https://doi.org/10.1162/neco.1997.9.8.1735, 1997.

Hu, H., van der Westhuysen, A. J., Chu, P., and Fujisaki-Manome, A.: Predicting Lake Erie wave heights and periods using XGBoost and LSTM, Ocean Model., 164, 101832, https://doi.org/10.1016/j.ocemod.2021.101832, 2021.

Hua, L., Zhang, C., Peng, T., Ji, C., and Shahzad Nazir, M.: Integrated framework of extreme learning machine (ELM) based 565 on improved atom search optimization for short-term wind speed prediction, Energ. Convers. Manage., 252, https://doi.org/10.1016/j.enconman.2021.115102, 2022.

Huang, J., Chen, Q., and Yu, C.: A New Feature Based Deep Attention Sales Forecasting Model for Enterprise Sustainable Development, Sustainability, 14, https://doi.org/10.3390/su141912224, 2022.

Huang, Y. and Deng, Y.: A new crude oil price forecasting model based on variational mode decomposition, Knowl-Based 570 Syst., 213, https://doi.org/10.1016/j.knosys.2020.106669, 2021.

Jain, P. and Deo, M. C.: Neural networks in ocean engineering, Ships Offshore Struc., 1, 25-35, https://doi.org/10.1533/saos.2004.0005, 2006.

Jain, P., Deo, M. C., Latha, G., and Rajendran, V.: Real time wave forecasting using wind time history and numerical model, Ocean Model., 36, 26-39, https://doi.org/10.1016/j.ocemod.2010.07.006, 2011.

575 Jamei, M., Ali, M., Karbasi, M., Xiang, Y., Ahmadianfar, I., and Yaseen, Z. M.: Designing a Multi-Stage Expert System for daily ocean wave energy forecasting: A multivariate data decomposition-based approach, Appl. Energ., 326, 119925,

https://doi.org/10.1016/j.apenergy.2022.119925, 2022.

Kamranzad, B., Etemad-Shahidi, A., and Kazeminezhad, M. H.: Wave height forecasting in Dayyer, the Persian Gulf, Ocean Engineering, 38, 248-255, https://doi.org/10.1016/j.oceaneng.2010.10.004, 2011.

580 Karbasi, M., Jamei, M., Ali, M., Abdulla, S., Chu, X., and Yaseen, Z. M.: Developing a novel hybrid Auto Encoder Decoder Bidirectional Gated Recurrent Unit model enhanced with empirical wavelet transform and Boruta-Catboost to forecast significant wave height, J. Clean. Prod., 379, 134820, https://doi.org/10.1016/j.jclepro.2022.134820, 2022.

Kok, C., Jahmunah, V., Oh, S. L., Zhou, X., Gururajan, R., Tao, X., Cheong, K. H., Gururajan, R., Molinari, F., and Acharya, U. R.: Automated prediction of sepsis using temporal convolutional network, Comput. Biol. Med., 127, 103957,
585 https://doi.org/10.1016/j.compbiomed.2020.103957, 2020.

Li, B., Zhang, J., He, Y., and Wang, Y.: Short-Term Load-Forecasting Method Based on Wavelet Decomposition With Second-Order Gray Neural Network Model Combined With ADF Test, IEEE Access, 5, 16324-16331, https://doi.org/10.1109/ACCESS.2017.2738029, 2017.

Li, H., Liu, T., Wu, X., and Chen, Q.: An optimized VMD method and its applications in bearing fault diagnosis, Measurement,
590 166, https://doi.org/10.1016/j.measurement.2020.108185, 2020.

Li, W., Wei, Y., An, D., Jiao, Y., and Wei, Q.: LSTM-TCN: dissolved oxygen prediction in aquaculture, based on combined model of long short-term memory network and temporal convolutional network, Environ. Sci. Pollut. Res. Int., 29, 39545-39556, https://doi.org/10.1007/s11356-022-18914-8, 2022a.

Li, X., Cao, J., Guo, J., Liu, C., Wang, W., Jia, Z., and Su, T.: Multi-step forecasting of ocean wave height using gate recurrent
595 unit networks with multivariate time series, Ocean Eng., 248, 110689, https://doi.org/10.1016/j.oceaneng.2022.110689, 2022b.

Liu, Y., Yang, C., Huang, K., and Gui, W.: Non-ferrous metals price forecasting based on variational mode decomposition and LSTM network, Knowl-Based Syst., 188, https://doi.org/10.1016/j.knosys.2019.105006, 2020.

Luo, Y., Shi, H., Zhang, Z., Zhang, C., Zhou, W., Pan, G., and Wang, W.: Wave field predictions using a multi-layer perceptron
600 and decision tree model based on physical principles: A case study at the Pearl River Estuary, Ocean Eng., 277, 114246, https://doi.org/10.1016/j.oceaneng.2023.114246, 2023.

Mafi, S. and Amirinia, G.: Forecasting hurricane wave height in Gulf of Mexico using soft computing methods, Ocean Eng., 146, 352-362, https://doi.org/10.1016/j.oceaneng.2017.10.003, 2017.

Makarynskyy, O.: Improving wave predictions with artificial neural networks, Ocean Eng., 31, 709-724,
605 https://doi.org/10.1016/j.oceaneng.2003.05.003, 2004.

Malekmohamadi, I., Ghiassi, R., and Yazdanpanah, M. J.: Wave hindcasting by coupling numerical model and artificial neural networks, Ocean Eng., 35, 417-425, https://doi.org/10.1016/j.oceaneng.2007.09.003, 2008.

Neshat, M., Nezhad, M. M., Sergiienko, N. Y., Mirjalili, S., Piras, G., and Garcia, D. A.: Wave power forecasting using an effective decomposition-based convolutional Bi-directional model with equilibrium Nelder-Mead optimiser, Energy, 256,
610 124623, https://doi.org/10.1016/j.energy.2022.124623, 2022.

Neumann and Pierson: A detailed comparison of theoretical wave spectra and wave forecasting methods, Dtsch. Hydrogr. Zeitschrift, 10, 73-92, 1957.

Ni, C. and Ma, X.: An integrated long-short term memory algorithm for predicting polar westerlies wave height, Ocean Eng., 215, 107715, https://doi.org/10.1016/j.oceaneng.2020.107715, 2020.

615 Nitsure, S. P., Londhe, S. N., and Khare, K. C.: Wave forecasts using wind information and genetic programming, Ocean Eng., 54, 61-69, https://doi.org/10.1016/j.oceaneng.2012.07.017, 2012.

Niu, D., Ji, Z., Li, W., Xu, X., and Liu, D.: Research and application of a hybrid model for mid-term power demand forecasting based on secondary decomposition and interval optimization, Energy, 234, https://doi.org/10.1016/j.energy.2021.121145, 2021.

620 Pushpam P., M. M. and Enigo V.S., F.: Forecasting Significant Wave Height using RNN-LSTM Models, In Proceedings of the 2020 4th International Conference on Intelligent Computing and Control Systems (ICICCS), 13–15 May 20202020.

Rao, A. D., Sinha, M., and Basu, S.: Bay of Bengal wave forecast based on genetic algorithm: A comparison of univariate and multivariate approaches, Appl. Math. Model., 37, 4232-4244, https://doi.org/10.1016/j.apm.2012.09.001, 2013.

Rasmussen, C. E.: Gaussian Processes in Machine Learning, in: Advanced Lectures on Machine Learning: ML Summer
625 Schools 2003, Canberra, Australia, February 2-14, 2003, Tübingen, Germany, August 4-16, 2003, Revised Lectures, edited by: Bousquet, O., von Luxburg, U., and Rätsch, G., Springer Berlin Heidelberg, Berlin, Heidelberg, 63-71,

https://doi.org/10.1007/978-3-540-28650-9_4, 2004.

Rogers, W. E., Hwang, P. A., and Wang, D. W.: Investigation of wave growth and decay in the SWAN model: Three Regional-Scale applications, J. Phys. Oceanogr., 33, 366-389, https://doi.org/10.1175/1520-0485(2003)033<0366:Iowgad>2.0.Co;2, 2003.

Shahriari, B., Swersky, K., Wang, Z., Adams, R. P., and de Freitas, N.: Taking the Human Out of the Loop: A Review of Bayesian Optimization, P. IEEE, 104, 148-175, https://doi.org/10.1109/jproc.2015.2494218, 2016.

Sverdrup, H. and Munk, W.: Wind, sea and swell. Theory of relations for forecasting, Navy Hydrographic office, Washington, DC, 601, 1947.

Tolman, H. L.: User manual and system documentation of WAVEWATCH III version 3.14, 2009.

Wamdi, G.: The WAM model—a third generation ocean wave prediction model, J. Phys. Oceanogr., 18, 1775–1810, https://doi.org/10.1175/1520-0485(1988)0182.0.CO;2, 1988.

Wang, W., Tang, R., Li, C., Liu, P., and Luo, L.: A BP neural network model optimized by Mind Evolutionary Algorithm for predicting the ocean wave heights, Ocean Eng., 162, 98-107, https://doi.org/10.1016/j.oceaneng.2018.04.039, 2018.

Wu, Q. and Lin, H.: Daily urban air quality index forecasting based on variational mode decomposition, sample entropy and LSTM neural network, Sustain. Cities Soc., 50, https://doi.org/10.1016/j.scs.2019.101657, 2019.

Xu, Y. H., Hu, C. H., Wu, Q., Li, Z. C., Jian, S. Q., and Chen, Y. Q.: Application of temporal convolutional network for flood forecasting, Hydrol. Res., 52, 1455-1468, https://doi.org/10.2166/nh.2021.021, 2021.

Yan, J., Mu, L., Wang, L., Ranjan, R., and Zomaya, A. Y.: Temporal Convolutional Networks for the Advance Prediction of ENSO, Sci. Rep., 10, 8055, https://doi.org/10.1038/s41598-020-65070-5, 2020.

Yu, Y., Si, X., Hu, C., and Zhang, J.: A Review of Recurrent Neural Networks: LSTM Cells and Network Architectures, Neural Comput., 31, 1235-1270, https://doi.org/10.1162/neco_a_01199, 2019.

Zhang, Q., Hu, W., Liu, Z., and Tan, J.: TBM performance prediction with Bayesian optimization and automated machine learning, Tunn. Undergr. Space Technol., 103, https://doi.org/10.1016/j.tust.2020.103493, 2020a.

Zhang, Y., Pan, G., Chen, B., Han, J., Zhao, Y., and Zhang, C.: Short-term wind speed prediction model based on GA-ANN improved by VMD, Renew. Energ., 156, 1373-1388, https://doi.org/10.1016/j.renene.2019.12.047, 2020b.

Zhang, Z., Wang, X., and Jung, C.: DCSR: Dilated Convolutions for Single Image Super-Resolution, IEEE Trans. Image Process., 28, 1625-1635, https://doi.org/10.1109/TIP.2018.2877483, 2019.

Zhao, W., Gao, Y., Ji, T., Wan, X., Ye, F., and Bai, G.: Deep Temporal Convolutional Networks for Short-Term Traffic Flow Forecasting, IEEE Access, 7, 114496-114507, https://doi.org/10.1109/access.2019.2935504, 2019.

Zhou, S., Bethel, B. J., Sun, W., Zhao, Y., Xie, W., and Dong, C.: Improving Significant Wave Height Forecasts Using a Joint Empirical Mode Decomposition–Long Short-Term Memory Network, J. Mar. Sci. Eng., 9, https://doi.org/10.3390/jmse9070744, 2021.

Zhou, T., Wu, W., Peng, L., Zhang, M., Li, Z., Xiong, Y., and Bai, Y.: Evaluation of urban bus service reliability on variable time horizons using a hybrid deep learning method, Reliab. Eng. Syst. Safe., 217, https://doi.org/10.1016/j.ress.2021.108090, 2022.

Zuo, G., Luo, J., Wang, N., Lian, Y., and He, X.: Decomposition ensemble model based on variational mode decomposition and long short-term memory for streamflow forecasting, J. Hydrol., 585, https://doi.org/10.1016/j.jhydrol.2020.124776, 2020.